Effect of Wedge-Shaped Deflectors on Flow Fields of Dual-Stream Jets

Rebecca S. Shupe[*]
University of California, Irvine, CA, 92697-3975

Khairul B. Zaman[†]
NASA Glenn Research Center, Cleveland, OH, 44135

Dimitri Papamoschou[‡]
University of California, Irvine, CA, 92697-3975

   The effect of wedge-shaped fan flow deflectors on the mean and turbulent flow-fields of dual-stream jets is investigated. Several wedge-shaped deflector concepts were used to create asymmetry in the plume of a dual-stream jet issuing from a scaled down version of the NASA Glenn '5BB' bypass-ratio 8 turbofan nozzle. The deflector configurations comprised internal and external wedges with and without a pylon. Some external wedges incorporated local extensions of the fan nacelle. All the deflectors reduced radial velocity gradients, magnitudes of peak Reynolds stresses, and peak turbulent kinetic energy beneath the jet centerplane, with an increase above the jet centerplane. A correlation was obtained between the maximum radial velocity gradient and the peak turbulent kinetic energy in the dominant noise source region.

Nomenclature

D	=	nozzle exit diameter
k	=	turbulent kinetic energy $= \dfrac{1}{2}\overline{(u'^2 + v'^2 + w'^2)}$
u,v,w	=	axial, vertical, and spanwise velocity components in jet plume
x,y,z	=	axial, vertical, and spanwise coordinates
U	=	velocity at jet exit
$(.)'$	=	fluctuating value
$\overline{(.)}$	=	mean (time-averaged) value

Subscripts

f	=	secondary (fan) stream
p	=	primary (core) stream
0	=	fixed axial location

[*]Graduate Student Researcher, Department of Mechanical and Aerospace Engineering, 4200 Engineering Gateway, Irvine, CA 92697-3975, and visiting Graduate Student Researcher at NASA Glenn Research Center, through the Graduate Student Researchers Program (GSRP) fellowship, AIAA Member.
[†]Aerospace Engineer, Propulsion Systems Division, Inlet and Nozzle Branch, 21000 Brookpark Road, M.S. 86-7, Cleveland, OH 44135, AIAA Associate Fellow.
[‡]Professor, Department of Mechanical and Aerospace Engineering, 4200 Engineering Gateway, Irvine, CA 92697-3975, AIAA Associate Fellow.

I. Introduction

This work is motivated by the advent of asymmetric dual-stream exhaust configurations for the suppression of airport community noise from turbofan engines. The specific method addressed here is the fan flow deflection (FFD) method, whereby aerodynamic devices are used to create asymmetry in the plume of a jet exiting an otherwise coaxial nozzle. The asymmetry causes noise reduction in the general direction of the deflection of the fan stream[1]. To appreciate the effect of the fan flow deflection, it is instructive to examine the principal features of the mean flow of a coaxial jet, sketched in Fig.1. They include the primary potential core, of length x_p, and the generalized secondary core (GSC) which forms around the primary core. The GSC is based on the outer two inflection points, i_2 and i_3, of the radial velocity profile, which naturally form a loop. The end of the loop, at $x=x_{GSC}$, signifies the transition of the velocity profile from dual-stream to single-stream. For the velocity ratios considered here, the initial region of the core jet surrounded by the GSC can be treated as "silent", in the sense that noise emission from the inner shear layer (between core and fan streams) is insignificant compared to the noise emission from the outer shear layer (between fan and ambient streams)[1,2]. Downstream of the GSC, the core stream contains the dominant sources of jet noise. Our present understanding of fan flow deflection is that it produces two major effects: lengthening of the GSC, thereby silencing a greater portion of the core flow; and/or reducing the radial velocity gradient past the end of the GSC.[3,4] For $x>x_{GSC}$, the maximum velocity gradient occurs on the locus of inflection points i_1, as shown in Fig. 1.

This work focuses on the reduction of the velocity gradient and its connection to changes in the turbulent velocity field. Two types of deflectors for creating asymmetry have been investigated so far: wedge-shaped deflectors mounted at the top of the nozzle, and airfoil-shaped vanes mounted at various azimuth angles[4-7]. Both devices can be internal or external to the fan duct, although vanes are more aerodynamically efficient when placed in the subsonic environment inside the fan duct. Figure 2 shows the placement of the wedge-shaped deflector. Past studies have shown that wedge-shaped deflectors, installed on a fan nozzle with convergent streamlines, have the potential to reduce jet mixing noise significantly, particularly in the direction of peak emission, for a range of azimuth angles without crossover at high polar angles.[4,5] Papamoschou and Shupe[4] noted a reduction in radial gradient of mean axial velocity component related to noise suppression in the downward direction in asymmetric bypass ratio 5 jets. In an effort to understand directional noise suppression due to a departure from symmetry of dual-stream jets, this work examines in detail the flow field characteristics affected by that departure, specifically changes in velocity gradients, turbulent kinetic energy, and Reynolds stresses.

II. Experimental Setup

Experiments were conducted in the CW-17 jet facility at NASA Glenn Research Center (GRC). Coannular flow is achieved via a secondary plenum chamber located just upstream of the nozzles. The secondary annular flow, supplied by four equally spaced ports, is routed through a contoured interior and screens to provide a uniform velocity profile at the exit. The primary Mach number at the exit was 0.18 and the secondary Mach number was 0.13. The secondary-to-primary velocity ratio was 0.7 representative of the velocity ratio of a turbofan exhaust at takeoff condition. However, the magnitudes of the velocities were much lower than in a real engine to enable the use of hot-wire techniques. In all experiments, air at room temperature was supplied to the separate-flow nozzle using a primary blower and an auxiliary blower. The auxiliary blower was mounted on a 2" by 8" support, custom crafted so that the blower outlet was flush mounted with existing piping.

A. Nozzle

The NASA GRC '5BB' nozzle has a bypass ratio of approximately 8 at typical engine cycle conditions. A scaled down version of this nozzle, with fan diameter D_f= 53.3 mm, was fabricated and used in the CW-17 facility. The Reynolds number of the jet, based on fan diameter, was 0.2×10^6. Exit conditions are listed in Tables 1-3 for the baseline nozzle. The 5BB nozzle has convergent exit flow lines for the fan and core ducts, typical of a realistic turbofan engine nozzle geometry. Figure 6 shows the radial coordinates of the 5BB nozzle. Photos of the nozzle are provided in Fig. 7.

B. Wedge and Pylon Configurations

Five different wedge designs were tested with and without a pylon. The wedges without pylon comprised two external wedges (W_1 and W_2) and two internal wedges (W_3 and W_4), as sketched in Fig. 3. W_1, W_2, and W_3 had half-angles of 15°. The height of the external wedge W_1 was twice the fan exit height (Fig. 3a). External wedge W_2, shown in Fig. 3b, had a height equal to fan exit height at its apex, gradually increasing to 1.25 times the fan exit height at its base. The cross sections of the external wedges are shown in Fig. 4. The internal wedge W_3, Fig. 3c,

used the same cross-section as the external wedges, Fig. 4a, and its contours were flush with the fan duct walls. Nacelle extensions of different geometries, Fig. 4c, were used to examine the effect of suppressing the flow upwash over the short external wedge W_2, resulting in the arrangements shown in Fig. 5a. Pylon configurations comprised a "wedge" W_4 that defined the interior portion of the pylon, and external pylon half-wedges or flaps. The cross-section of W_4 was fast-diverging wedge deep inside the fan duct, with a half angle of roughly 30°, with the sides becoming parallel to one another close to the fan exit, as shown in Fig. 4b. The external, pylon-mounted half-wedges had angles of 7 deg. relative to the pylon surface.

Figure 6 plots the coordinates of the base nozzle and with wedges $W_1 - W_4$ installed. Figure 7 shows photographs of the external wedge configurations tested, including the pylon with external half wedges. Wedges $W_1 - W_3$ were fabricated using Duraform EX plastic material. The pylon was constructed of three plastic pieces. The ensemble comprised an internal component (W_4), terminating at the fan exit plane, an external component that was flush-mounted against the internal component, and two side-mounted half wedges (Fig.5b).

C. Velocity Measurements

Two pairs of crossed hot-wires, illustrated in Fig. 8, were used to survey the mean and fluctuating velocity components in the jet plume. One was in a u-v configuration, the other in a u-w configuration. The wires were spaced 1.0-mm apart, limiting the spatial resolution to 1.0 mm in the y- and z-directions. The probes were mounted on a streamlined strut, visible in Fig. 7a, and the positioning was automated under computer control in all three directions. The two probes were located at the same y-location (vertical) and spaced apart from one another by 23-mm in the z-direction (spanwise), Fig. 8. The step size in the z-direction was chosen to be a submultiple of the separation distance so that a shift of the u-v probe data by an integral number of steps matched the corresponding data from the u-w probe.

With increasing axial distance, both the spatial resolution and the sampling rate were decreased. Smaller grid intervals were used where sharp spatial gradients were expected in the initial region of the jet. An exponential function was used to decrease the spatial resolution with axial distance. In the x-direction, 16 data points were acquired, spanning $8.23D_f$. Grid spacing in the x-direction started with a separation of $0.114D_f$ or 6.1-mm between the first and second data points and ended with a separation of $1.47D_f$ between the last two data points. The first data point was taken $0.024D_f$ from the tip of the nozzle center plug in x and $0.62D_f$ from the jet centerline in y, where the velocity was small. For each axial station, 19 data points were collected along y, uniformly spaced. At each axial station, the grid spacing in y was adjusted so that the outer grid points formed an angle of 5.35^o with the axis. The upstream-most position used uniform intervals of $0.0715D_f$ (3.8-mm) and the furthest position downstream used uniform intervals of $0.157D_f$ (8.3-mm). For distances upstream of $4.28D_f$, the sampling rate used was 500 Hz, and for distances downstream of $4.28D_f$ from the plug tip, the sampling rate used was 200 Hz. The ensemble size was 2000. Thus, sampling times of 4s or 10s were used depending on the axial location. At each grid point, all three components of mean and RMS velocities were obtained. The Reynolds stresses $\overline{u'v'}$ and $\overline{u'w'}$ were also measured.

In addition to the crossed wire surveys, a single wire was used separately to survey the nozzle exit boundary layers. The boundary layers were found to be nominally laminar and their characteristics are listed in Table 3; here, location 1 refers to the inner layer of the primary (core) nozzle, location 2 refers to the outer layer of the primary (core) nozzle, and location 3 refers to the inner layer of the secondary (fan) nozzle.

III. Results

A. Mean and RMS Velocity Fields

Figure 9 shows the isocontours of the mean axial velocity, normalized by the primary exit velocity, for the baseline jet and for the wedge configurations $W_1 - W_3$. Note the reduction in potential core for all the wedge cases, by examining the contour level $\bar{u}(x,y,0)/U_p$=0.9. Since the potential core length, x_p, provides a scaling for the volume of turbulent mixing noise sources in jets, it is desirable to reduce it. Table 4 lists potential core lengths for the baseline jet and for each asymmetric dual-stream jet, based on 90% of the primary jet exit velocity U_p. The internal wedges are particularly effective in reducing x_p. In Fig. 9, cross-sectional slices of the jet plume are shown at the plug tip, x_0/D_f=1, and near the end of the primary potential core, x_0/D_f=5. The values of x are referenced to the secondary (fan) nozzle exit plane. Uniformly reduced gradients beneath the jet centerplane are observed, similar to those reported in Ref. 4. The cross-sectional slices at x_0/D_f=1 for the two external wedges show that there is a wake region behind the wedge. Studies have shown that the drag for a wedge placed in a jet stream with the top surface exposed to ambient fluid is 75% less than the drag of the classical two-dimensional wedge problem.[8]

Figures 10 and 11 depict isocontours of the RMS axial velocity fluctuation for the baseline jet and for all the isolated (without pylon) wedge configurations. It is noted that all the wedge configurations reduce the RMS levels below the jet centerplane and increase them above the jet centerplane. Internal wedges generally increase the RMS levels on the upper side of the jet much more than do external wedges. Thus, the enhanced mixing of the internal wedge, evident by the significant reduction of potential core length, comes at the expense of a large increase in turbulence levels at the top of the jet (Fig. 10d-e). Figure 11 shows that a nacelle extension to the external wedge may further reduce turbulence intensity on the underside of the jet, with the tradeoff of increased levels on the upper side of the jet.

B. Turbulent Kinetic Energy and Reynolds Stresses

Figure 12 shows isocontours of the mean velocity, turbulent kinetic energy, and Reynolds stress $\overline{u'v'}$ for the baseline jet and for the external wedge configurations W_1 and W_2. Corresponding to a reduction in radial gradient in the downward direction, there is a reduction in peak turbulent kinetic energy (TKE) and a reduction in magnitude of peak Reynolds stress underneath the jet centerplane. There is a tradeoff of an increase in peak TKE and peak Reynolds stress above the jet centerplane. Tables 4 and 5 list the peak values of TKE and Reynolds stresses on the upper and lower half-planes of the jet.

Figure 13 shows the mean velocity, turbulent kinetic energy, and Reynolds stress $\overline{u'v'}$ isocontours for the baseline jet and the internal wedge configurations W_3 and W_4. The trends are similar, but more pronounced, as for the external wedges.

Figure 14 shows the mean velocity, turbulent kinetic energy, and Reynolds stress $\overline{u'v'}$ isocontours for the baseline jet and the internal pylon portion W_4, with and without the external pylon, and with an external pylon and flaps. The outer pylon increases the magnitude of the peak Reynolds stress beneath the jet by approximately 10% when compared with the inner portion W_4 alone. The addition of external flaps reduces the magnitude of the peak Reynolds stresses by about 15% relative to the configuration W_4 + **Pylon**. Ref. 9 provides a nice discussion on sensitivity of flow field to jet-pylon interaction. The external flaps provide a net reduction in the magnitude of peak Reynolds stress, suggesting the potential of external flaps for noise suppression on a separate-flow turbofan engine.

With regard to the Reynolds stress $\overline{u'w'}$, Table 5 shows that the external wedges W_1, W_2, and W_2 + **Cap 1** resulted in a decrease in its peak magnitude. This may indicate that the external wedges have better capability to reduce noise in the sideline direction, compared to the other configurations presented. Acoustic measurements are needed to confirm this.

C. Correlation Between Turbulent Kinetic Energy and Radial Velocity Gradient

We now discuss the connection between radial velocity gradient and turbulent kinetic energy. Figures 15 and 16 plot the loci of inflection points, axial distributions of the radial velocity gradient along inflection point i_1 on the underside of the jet (Fig.1). Also shown are the axial distribution of peak TKE on the underside of the jet for all the configurations without the pylon. As mentioned in the introduction, the outer inflection points, i_2 and i_3, define the generalized secondary core (GSC). The maximum radial velocity gradient occurs on the inflection point i_1 past the end of the GSC. Figure 15 covers configurations $W_1 - W_4$, with the reference being the baseline nozzle. Figure 16 covers the W_2 + **Caps** configurations and the reference is case W_2. We observe generally an elongation of the GSC beneath the jet centerplane and a shortening of the GSC above the jet centerplane. In the baseline jet, it is evident that there is some asymmetry in the flow despite painstaking efforts to align the nozzle. Corresponding to the jet asymmetry, or the thickening of low-speed fluid underneath the jet, are reduced radial velocity gradients in the downward hemicylinder of the jet, and reduced peak TKE levels.

Figure 17 shows a correlation between the radial gradient of the axial velocity component measured at the end of the GSC, defined as

$$G = \frac{\partial \overline{u}(x_{GSC}, y_{i1}, 0)}{\partial y} \cdot \frac{D_f}{U_p}, \tag{1}$$

and the peak value of the turbulent kinetic energy. The correlation encompasses both the lower and upper sides of the jet. Because the baseline case was not perfectly symmetric, two points are obtained for the baseline, one above, and one below the jet centerplane. A regression of the form $k/U_p^2 = 0.000884G^2 - 0.002621G + 0.002955$, is valid both above and below the jet centerplane.

Since the peak turbulent kinetic energy can be thought of as a measure of how intense the turbulent mixing is, it is logical that it should also provide a measure for turbulent mixing noise. Therefore, this correlation yields insight into the important mean flow parameter that will yield a correlation with noise. This is important, since a large number of experiments have been conducted at UCI for which there are only mean flow measurements to be

correlated with the noise measurements. The direct correlation between the mean flow parameter measured at the end of the generalized secondary core and the peak turbulent kinetic energy suggests that it may be possible to obtain a correlation, a topic of future research.

In constructing correlations with the acoustics, the gradient parameter

$$G = \frac{\partial \overline{u}(x_{GSC}, y_{i1}, 0)}{\partial y} \cdot \frac{x_p}{U_p}, \tag{2}$$

may be more physical because it is based on the potential core length, x_p, which defines roughly the extent of the core noise sources. Figure 18 shows a promising correlation. Hopefully, this parameter may be used to correlate downward reductions in overall sound pressure level, although current models are still preliminary. One of the remaining challenges in obtaining a robust correlation between acoustics and mean flow will be to extend the procedure to include the azimuthal variations of the velocity gradient and of the GSC.

IV. Conclusions

Flow field surveys at NASA Glenn Research Center were conducted in an effort to understand and quantify the effects of wedge-shaped fan flow deflectors on the mean and turbulent velocity fields of dual-stream jets. A large variety of such deflectors was tested on a scaled-down version of the GRC 5BB nozzle, including internal and external wedges. We focused on the distributions of radial velocity gradients, peak turbulent kinetic energy, and peak Reynolds stresses, on the jet plane of symmetry. Crossed hot-wire measurements revealed reductions of the aforementioned parameters on the underside of the jet and increases on the upper side of the jet. External wedges provided significant downward reduction in turbulence levels with the least amount of upward increases. The experiments were instrumental in establishing a link between the asymmetry of the mean velocity field and the reduction in peak turbulent kinetic energy and peak Reynolds stresses. Reduced velocity gradients were correlated with reduced turbulent kinetic energy levels. This correlation is hoped to help in the development of models connecting noise reduction to the distortion of the mean flow. Through computational flow field predictions, it would enable the efficient design of next-generation aircraft engine nozzles with directional noise suppression capabilities.

Acknowledgments

References

[1] Papamoschou, D., "New Method for Jet Noise Suppression in Turbofan Engines," *AIAA Journal*, Vol. 42, No.11, 2004, pp. 2245-2253.

[2] Fisher, M.J., Preston, G.A., and Bryce, W.D., "A Modelling of the Noise from Simple Coaxial Jets, Part 1: With Unheated Primary Flow," *Journal of Sound and Vibration*, Vol. 209, No. 3, 1998, pp. 385-403.

[3] Papamoschou, D., "Mean Flow and Acoustics of Dual-Stream Jets," *AIAA Paper* 2004-0004, presented at the 42nd AIAA Aerospace Sciences Meeting, January 2004, Reno, NV.

[4] Papamoschou, D., and Shupe, R.S., "Effect of Nozzle Geometry on Jet Noise Reduction using Fan Flow Deflectors," *AIAA Paper* 2006-2707, presented at the 12th AIAA/CEAS Aeroacoustics Conference, Cambridge, MA, May 8-10, 2006.

[5] Papamoschou, D., "Fan Flow Deflection in Simulated Turbofan Exhaust," *AIAA Journal*, Vol. 44, No.12, 2006, pp. 3088-3097.

[6] Zaman, K.B.M.Q., Bridges, J. E., and Papamoschou, D., "Offset Stream Technology Comparison of Results from Experiments Conducted at UCI and GRC," *AIAA Paper* 2007-0438, January 2007.

[7] Henderson, B., Norum, T. and Bridges, J. E., "An MDOE Assessment of Nozzle Vanes for High Bypass Ratio Jet Noise Reduction," *AIAA Paper* 2006-2543, presented at the 12th AIAA/CEAS Aeroacoustics Conference, Cambridge, MA, May 8-10, 2006.

[8] Papamoschou, D. Vu, A., and Johnson, A.J., "Aerodynamics of Wedge-Shaped Deflectors for Jet Noise Reduction," *AIAA Paper* 2006-3655, presented at the 24th AIAA Applied Aerodynamics Conference, June 2006, San Francisco, CA.

[9] Birch, S.F., Lyubimov, D.A., Buchshtab, P.A., Secundov, A.N. and Yakubovsky, K.Y., "Jet-Pylon Interaction Effects", *AIAA Paper* 2005-3082, 11th Aeroacoustics Meeting, Monterey, CA, 23-25 May, 2005.

Table 1 GRC 5BB Nozzle Parameters

Quantity	Primary	Secondary
Nozzle diameter (mm)	27.2	53.27
Plug diameter (mm)	20.4	-
Lip thickness (mm)	0.70	-
Protrusion (mm)	25.3	-

Table 2 GRC 5BB Nozzle Exit Conditions

Quantity	Primary	Secondary
Velocity (m/s)	63.1	44.2
Mach number	0.18	0.13
Bypass ratio	-	2.67

Table 3 GRC 5BB Nozzle Boundary Layer Surveys

Boundary Layer Survey Location	Momentum thickness, δ_2 (in.)	Displacement thickness, δ_l (in.)	Shape factor, δ_l/δ_2	Maximum turbulence, u'_{max}/U_p
1. Inner Primary Nozzle	0.0017	0.0040	2.36	0.017
2. Outer Primary Nozzle	0.0032	0.0079	2.50	0.057
3. Inner Fan Nozzle	0.0017	0.0017	2.46	0.015

Table 4   Peak TKE and Mean Flow Field Parameters

GRC Experiment	Peak k/U_p^2 Below	Peak k/U_p^2 Above	$*G$ Below	$*G$ Above	x_{GSC}/D_f Below	x_{GSC}/D_f Above	x_p/D_f
Baseline	0.0172	0.0154	2.27	2.30	2.22	2.66	5.79
W1	0.0142	0.0164	2.14	2.36	2.26	1.19	5.13
W2	0.0144	0.0168	2.15	2.42	2.23	1.14	5.30
W3	0.0103	0.0206	1.70	2.49	3.55	1.00	4.40
W4	0.0144	0.0179	2.22	2.45	2.15	1.00	5.17
W2+Cap1	0.0134	0.0179	2.08	2.45	2.35	1.12	5.14
W2+Cap2	0.0135	0.0208	2.10	2.51	2.36	1.00	4.71
W2+Cap3	0.0140	0.0163	2.10	2.41	2.33	1.15	5.33

$$* \ G = \frac{\partial \bar{u}\left(x_{GSC}, y_{i1}, 0\right)}{\partial y} \cdot \frac{D_f}{U_p}$$

Table 5 Peak Reynolds Stresses

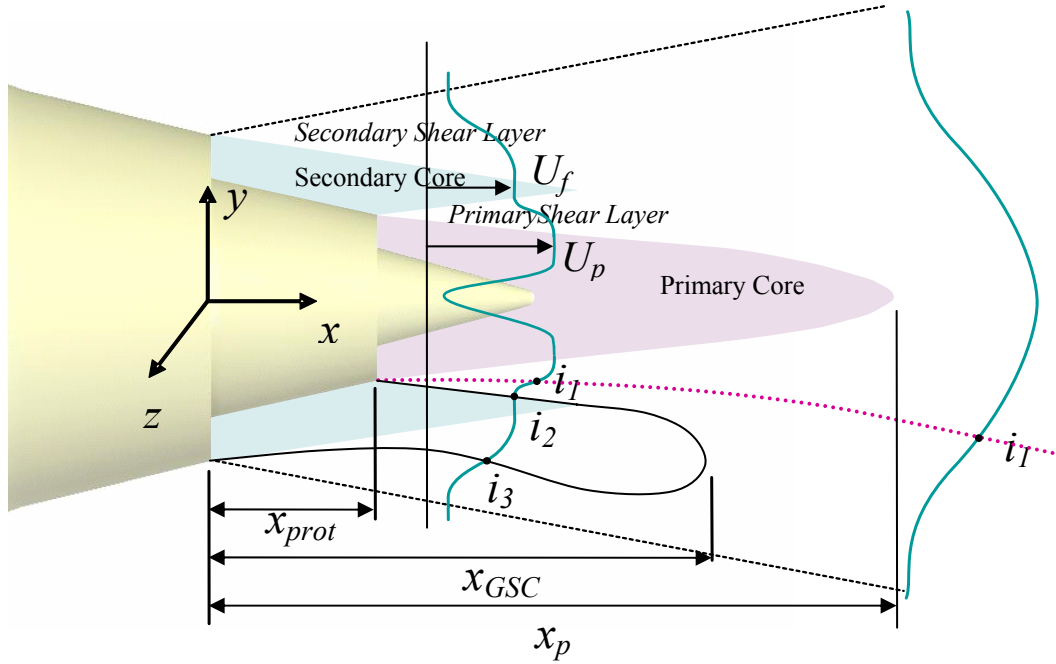| GRC Experiment	Peak $\overline{u'v'}/U_p^2$ Below (-)	Peak $\overline{u'v'}/U_p^2$ Above (+)	Peak $\overline{u'w'}/U_p^2$ (-)	Peak $\overline{u'w'}/U_p^2$ (+)
Baseline	-0.00427	0.00368	-0.00505	0.00425
W1	-0.00388	0.00569	-0.00480	0.00425
W2	-0.00399	0.00509	-0.00411	0.00398
W2+Cap1	-0.00398	0.00479	-0.00422	0.00400
W3	-0.00330	0.00529	-0.00570	0.00609
W4	-0.00379	0.00489	-0.00490	0.00450
W4+Pylon	-0.00417	0.00434	-0.00493	0.00470
W2+Pylon+Flaps	-0.00358	0.00500	-0.00616	0.00560

Fig. 1 Primary potential core length, x_p, generalized secondary core (GSC) length, x_{GSC}, and protrusion of inner nozzle, x_{prot}. The GSC is formed by outer inflection points i_2 and i_3. Maximum velocity gradient is considered on i_1 for $x \geq x_{GSC}$.
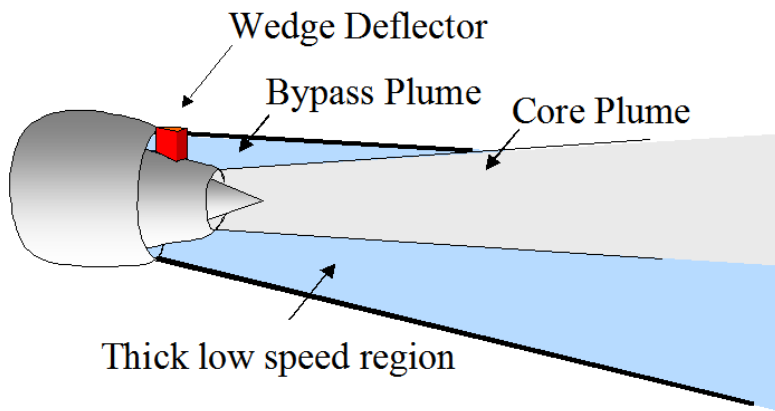

Fig. 2 Wedge-shaped deflector and thickened low speed region underneath the jet centerplane.
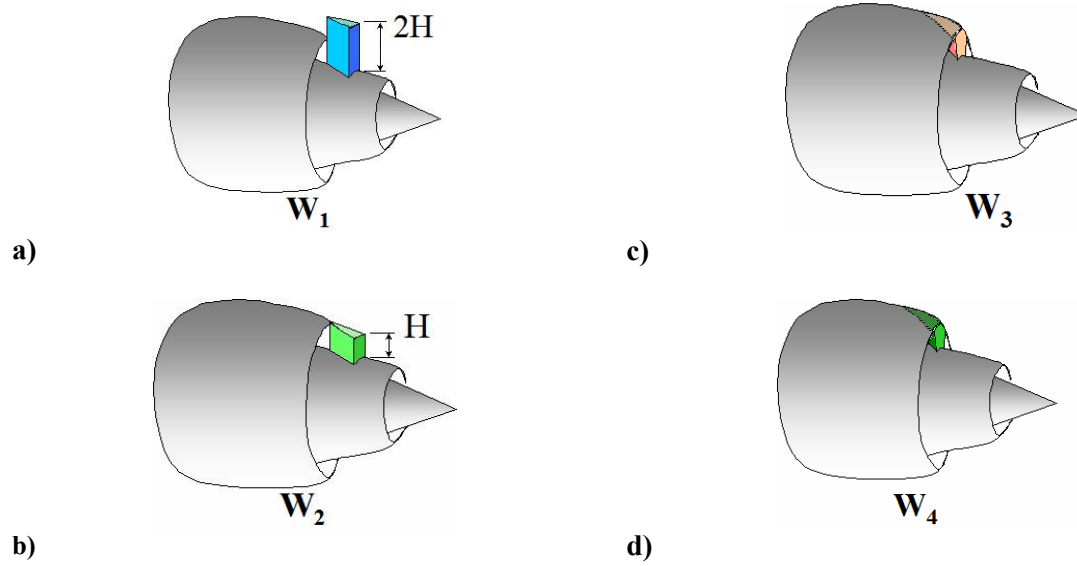
American Institute of Aeronautics and Astronautics

Fig. 3 **Wedge-shaped deflector configurations. a) W_1 b) W_2 c) W_3 and d) W_4. H = 6.83 mm is the fan exit height.**
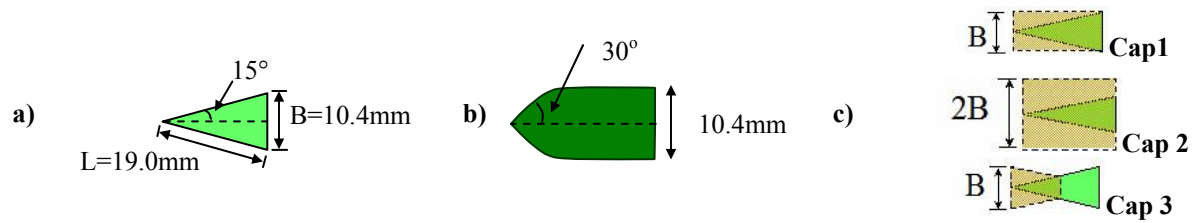
Fig. 4 **Cross-sections of a) W_1, W_2, and W_3 ; b) W_4 ; and c) three caps (top views).**
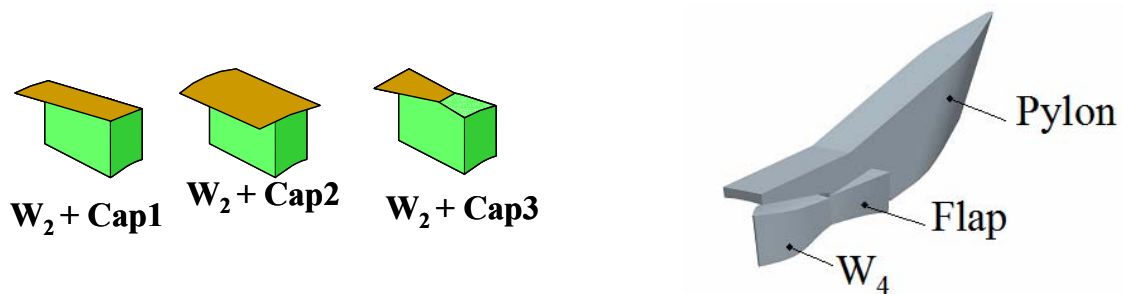
Fig. 5 **a) Cap configurations tested. b) W_4 + pylon + external flap.**
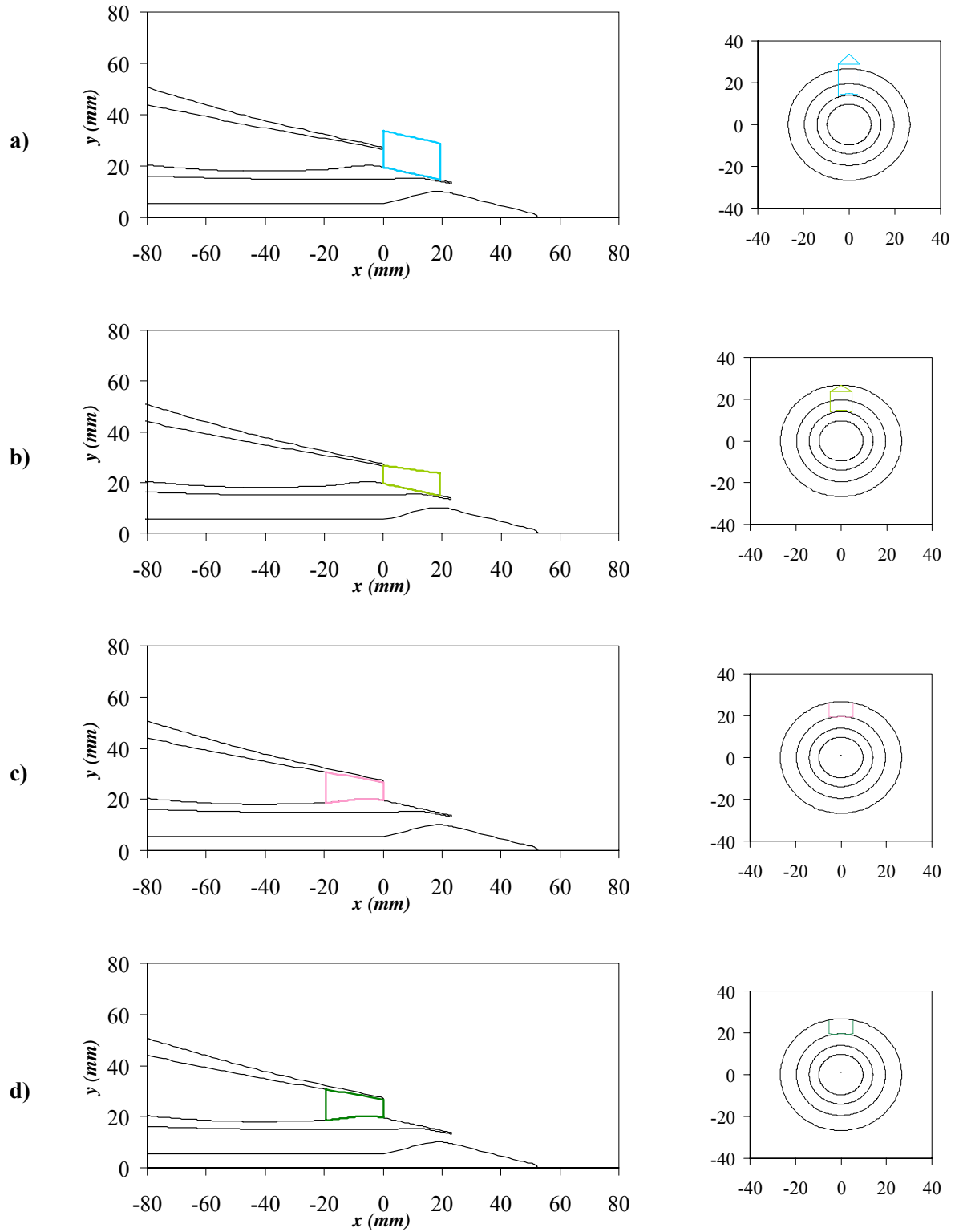
Fig. 6   Radial coordinates for the CW17 '5BB' nozzle with a) W_1 ; b) W_2 ; c) W_3 ; and d) W_4.
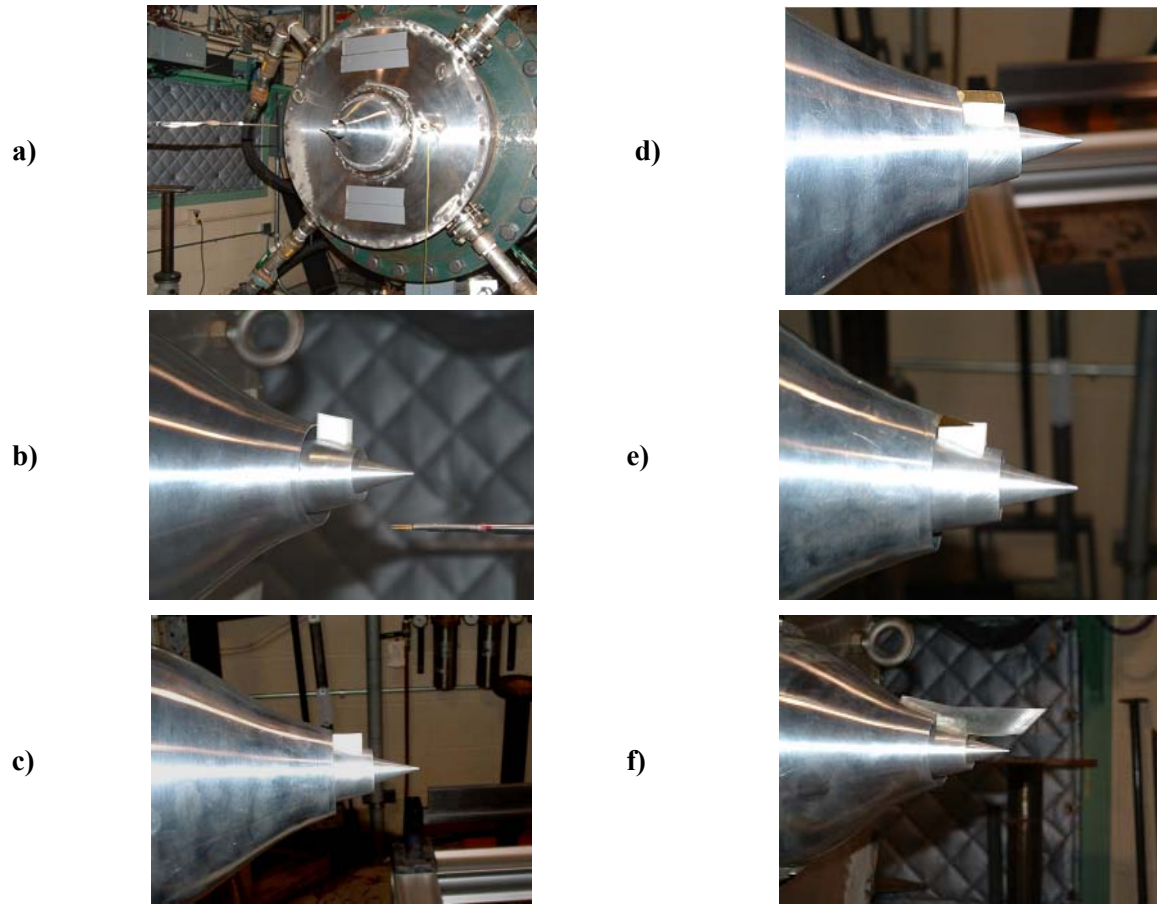
Fig. 7   Photos of a) GRC CW-17 jet facility with '5BB' nozzle. Crossed hot-wire probes mounted on an arm attached to a 3D traversing mechanism are in the foreground. b) W_1; c) W_2; d) W_2 + Cap 1; e) W_2 + Cap 3; f) W_4 + Pylon + Flaps.
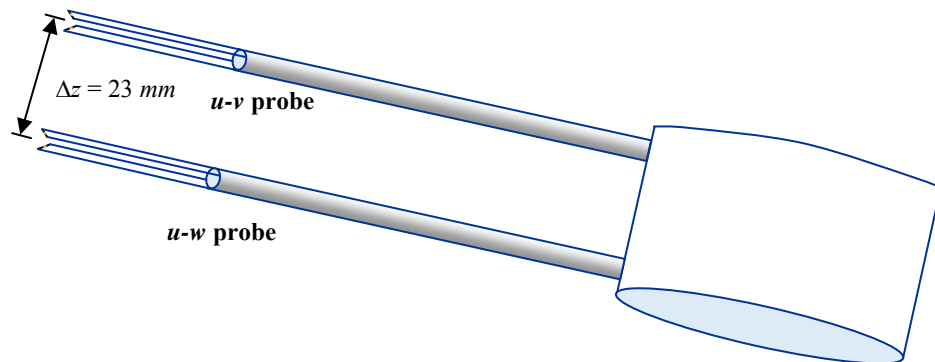
Fig. 8   Illustration of *u-v* and *u-w* crossed hot-wire probe, showing separation in the *z*-direction.
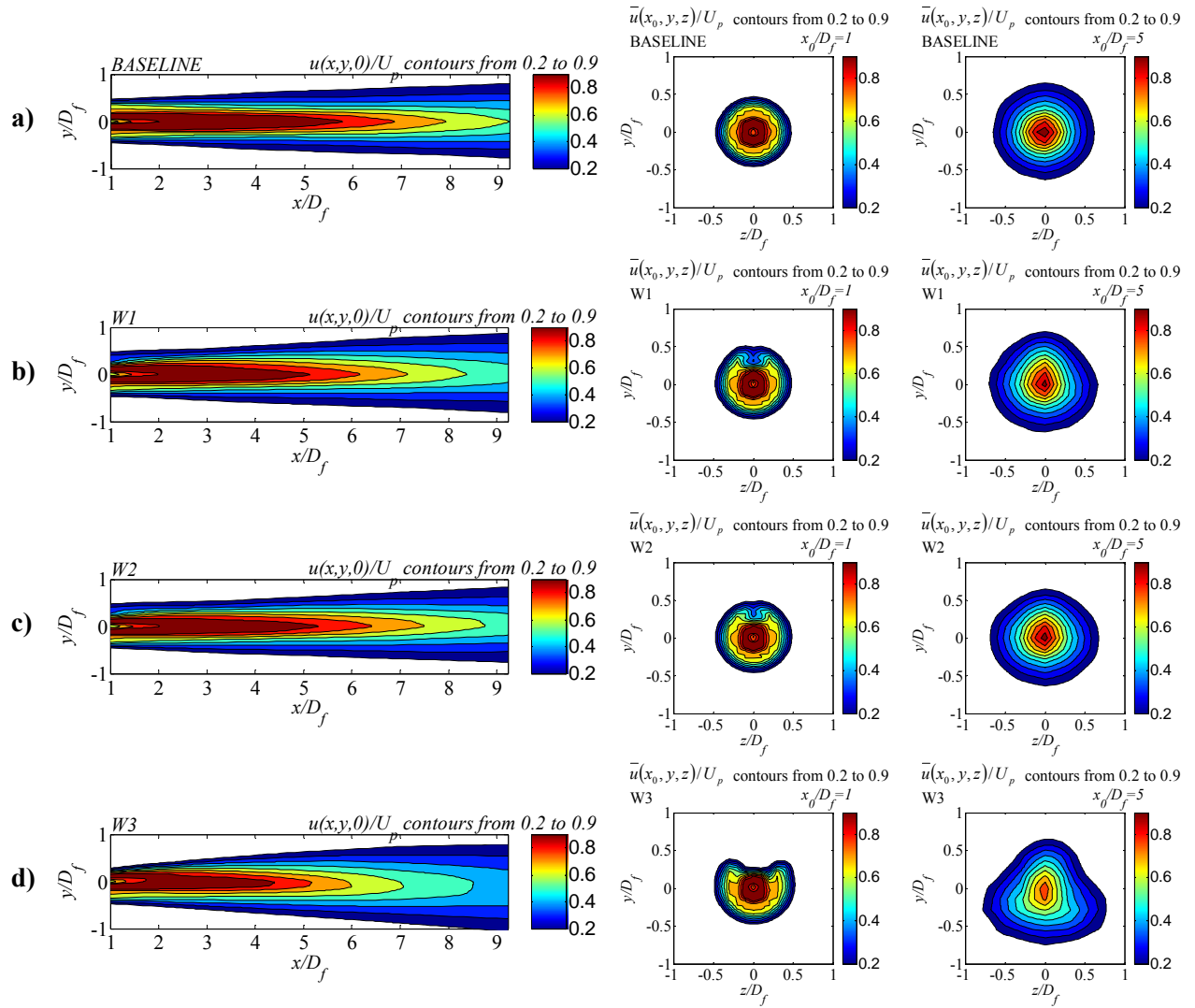
Fig. 9 Isocontours of mean axial velocity on the planes $z=0$, $x/D_f=1$, and $x/D_f=5$. a) Baseline nozzle; b) external wedge W_1; c) external wedge W_2; and d) internal wedge W_3.

American Institute of Aeronautics and Astronautics
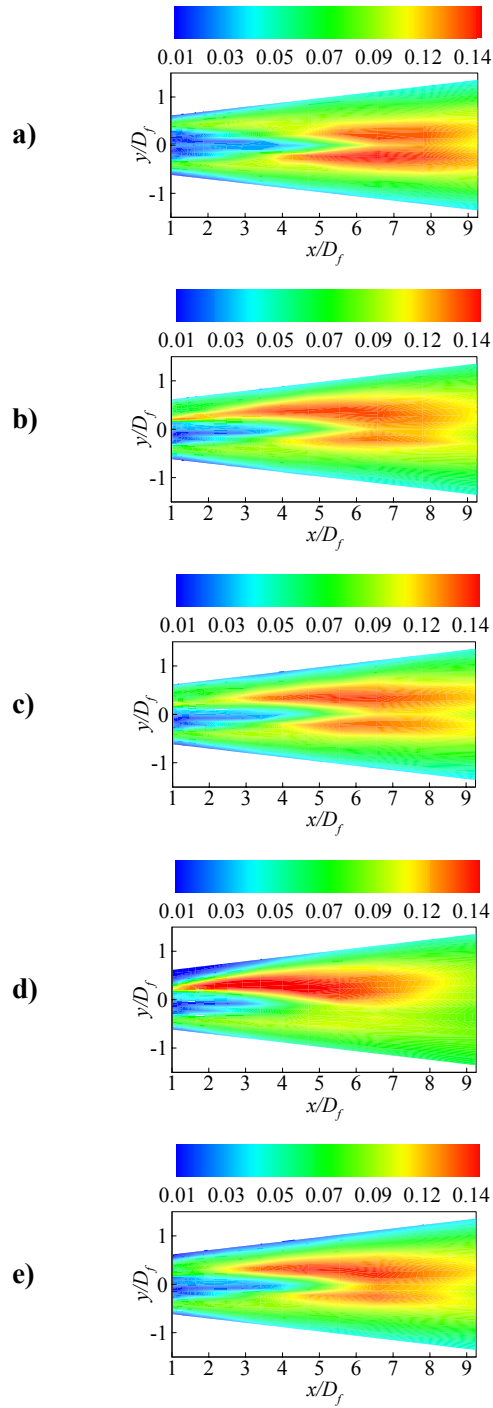
Fig. 10   RMS axial velocity fluctuation on the plane $z=0$ for: a) baseline nozzle; b) W_1; c) W_2 ; d) W_3 ; and e) W_4.
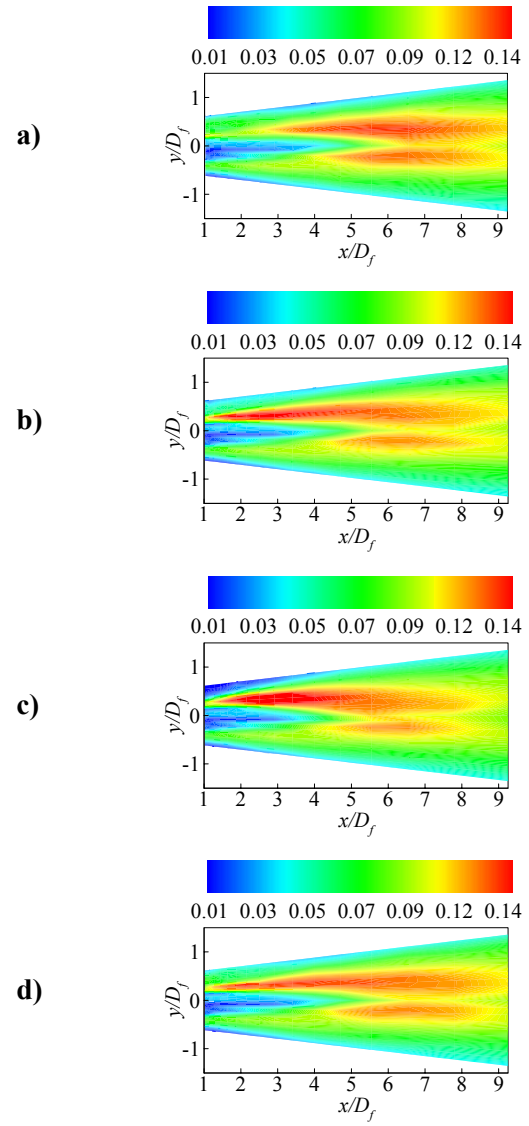
Fig. 11 RMS axial velocity fluctuation on the plane $z=0$ for: a) W_2; b) W_2 + Cap 1; c) W_2 + Cap 2; and d) W_2 + Cap 3.
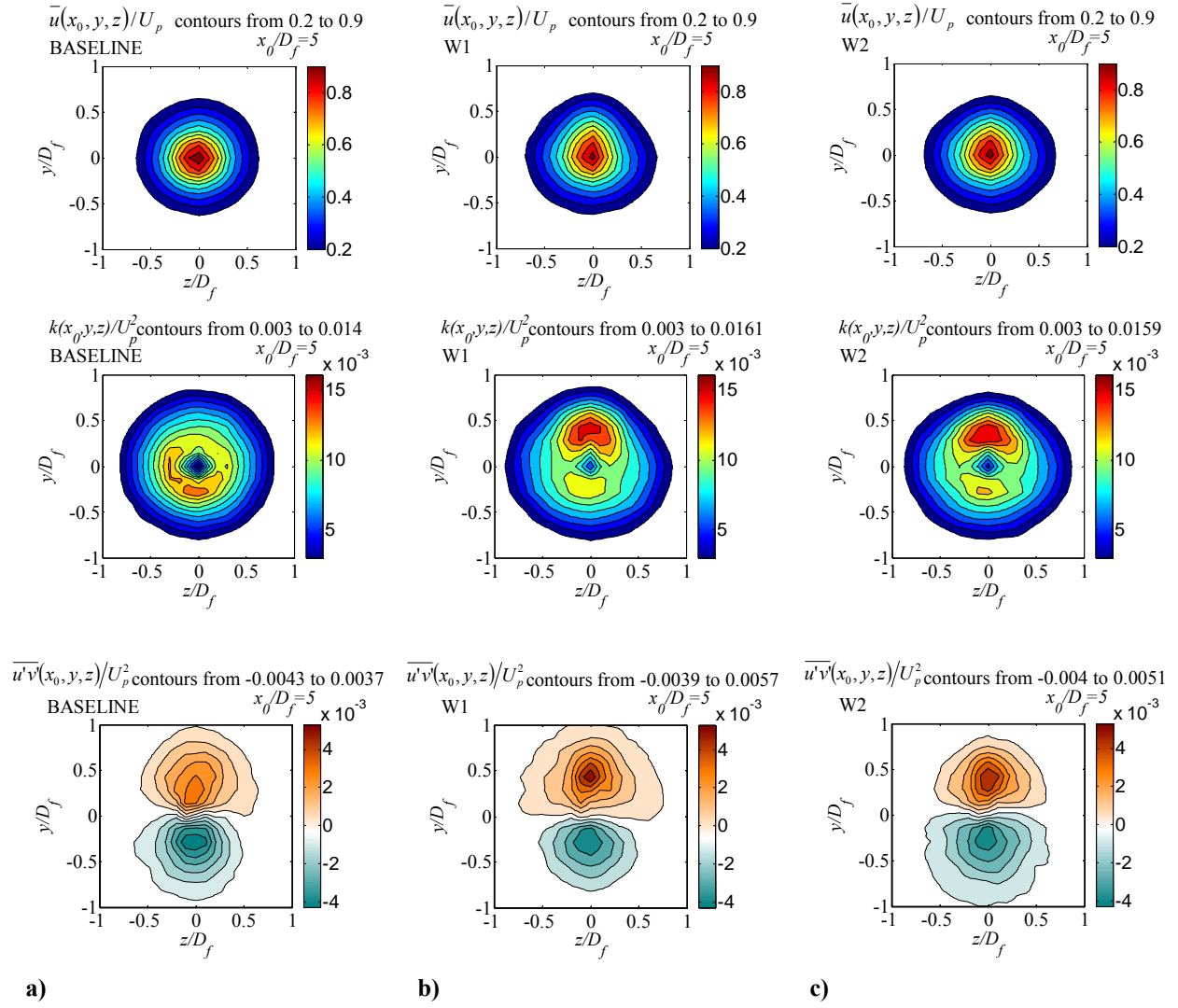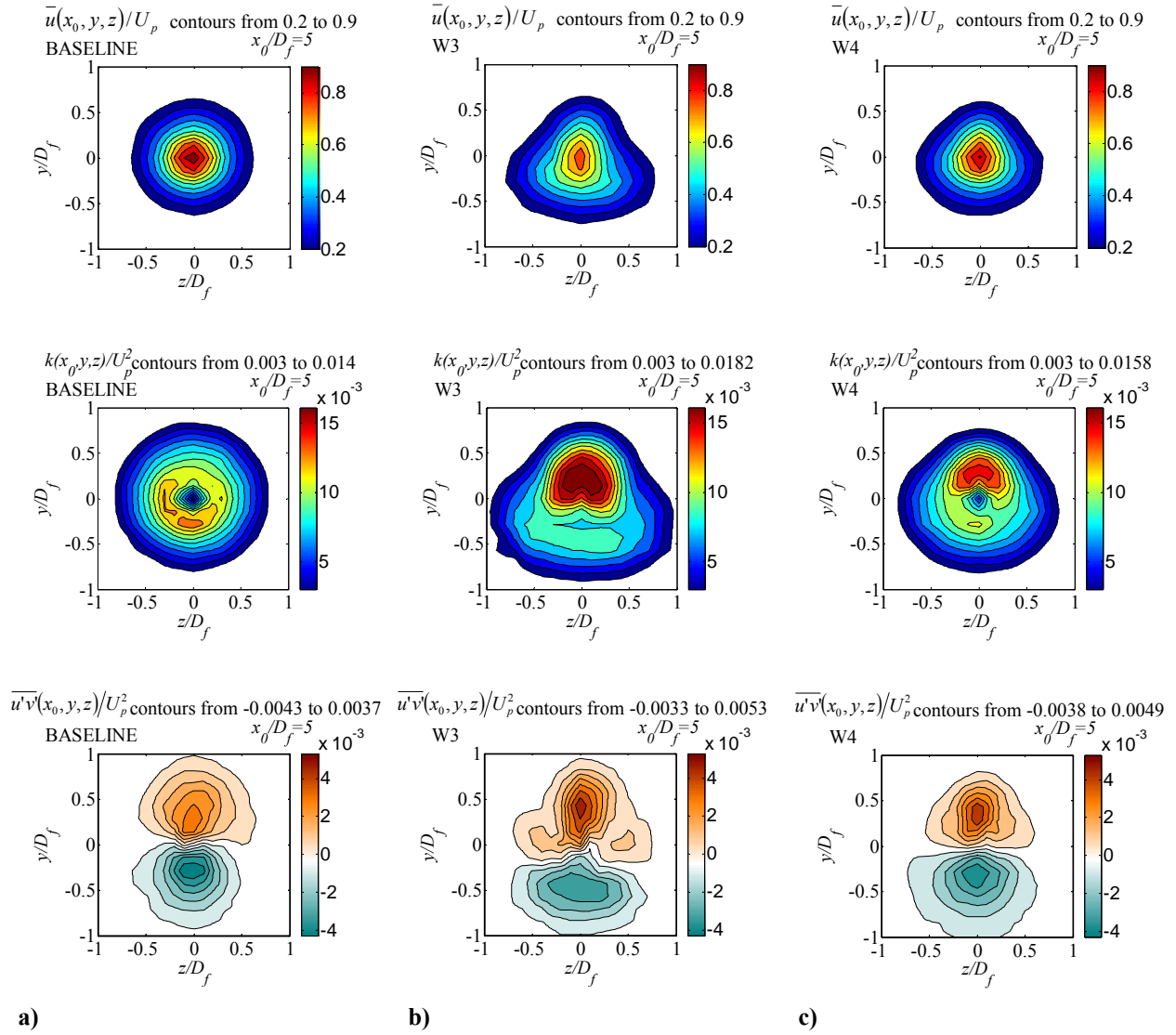
Fig. 12 Cross-sectional isocontours at x/D_f=5 of mean velocity (top), turbulent kinetic energy (middle), and Reynolds stress (bottom). a) Baseline nozzle; b) W_1; and c) W_2.
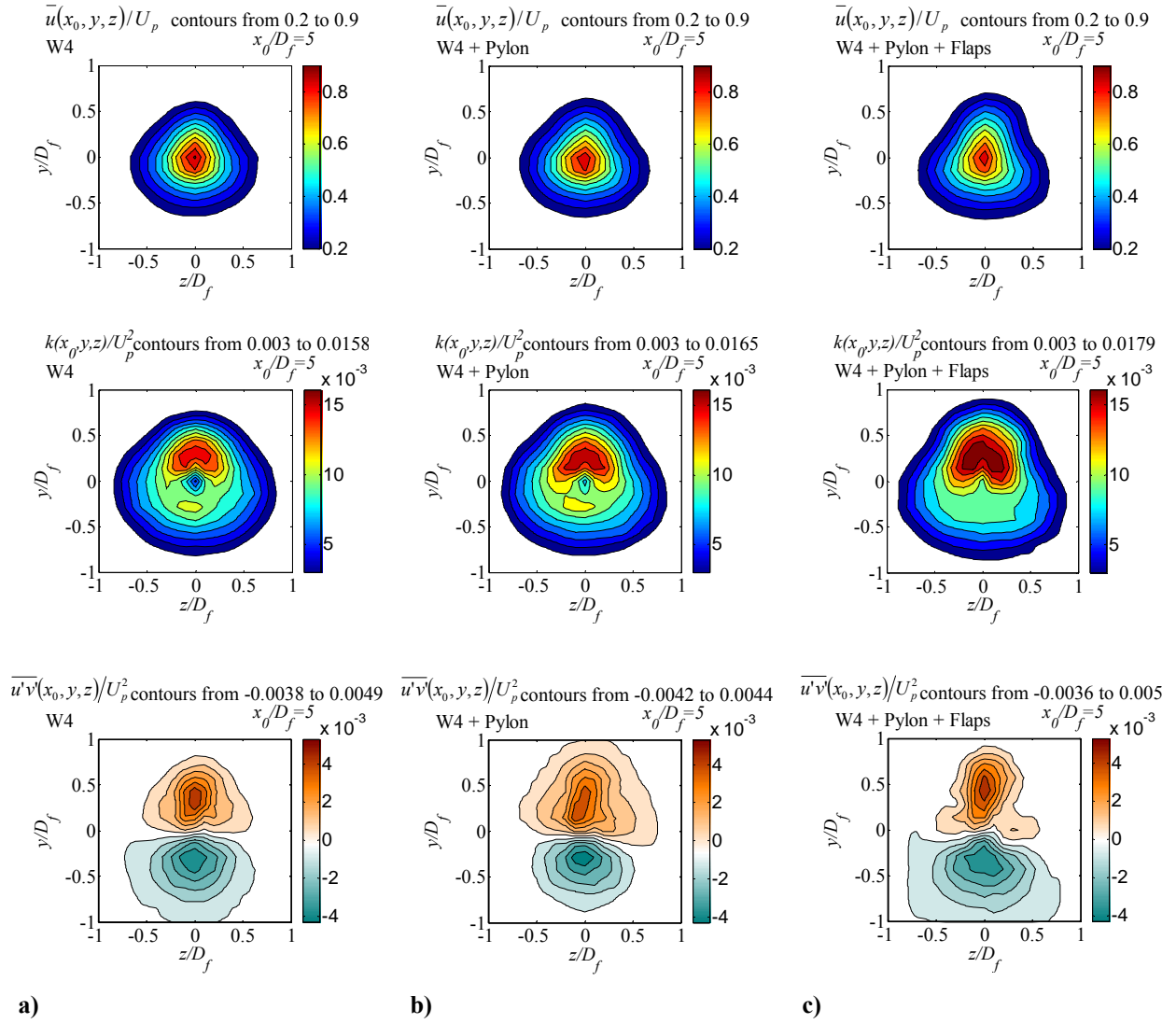
Fig. 13 Cross-sectional isocontours at x/D_f=5 of mean velocity (top), turbulent kinetic energy (middle), and Reynolds stress (bottom). a) Baseline nozzle; b) W_3; and c) W_4.

Fig. 14 Cross-sectional isocontours at x/D_f=5 of mean velocity (top), turbulent kinetic energy (middle), and Reynolds stress (bottom). a) W4; b) W_4 + Pylon; and c) W_4 + Pylon + Flaps.
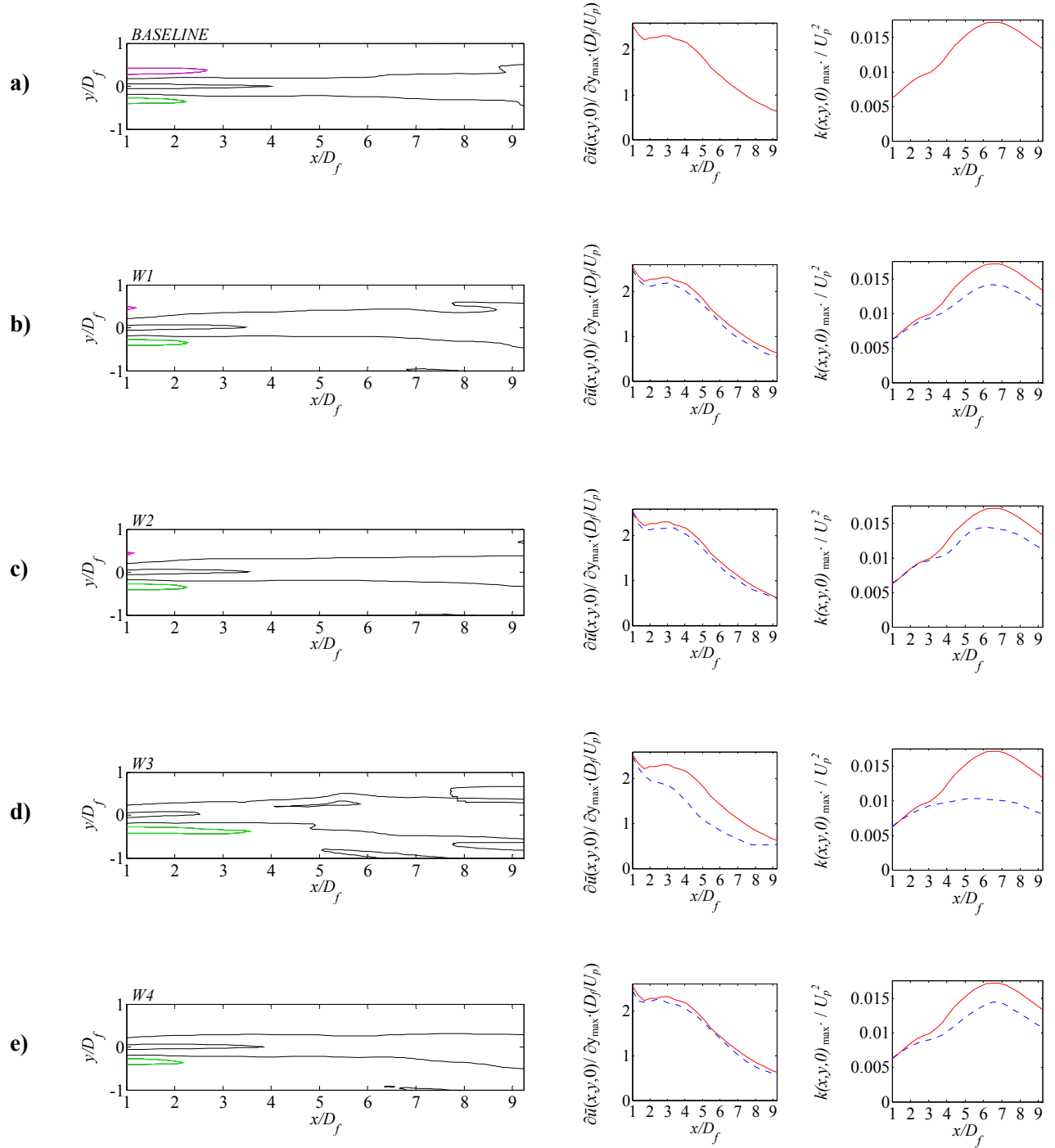
Fig. 15   Inflectional loci showing GSC below jet — and GSC above jet — (left); maximum radial gradient of the axial component of velocity (middle); and maximum turbulent kinetic energy below jet centerplane (right). a) Baseline; b) W_1; c) W_2; d) W_3; and e) W_4.. (Baseline — ; Wedge Cases - - -).
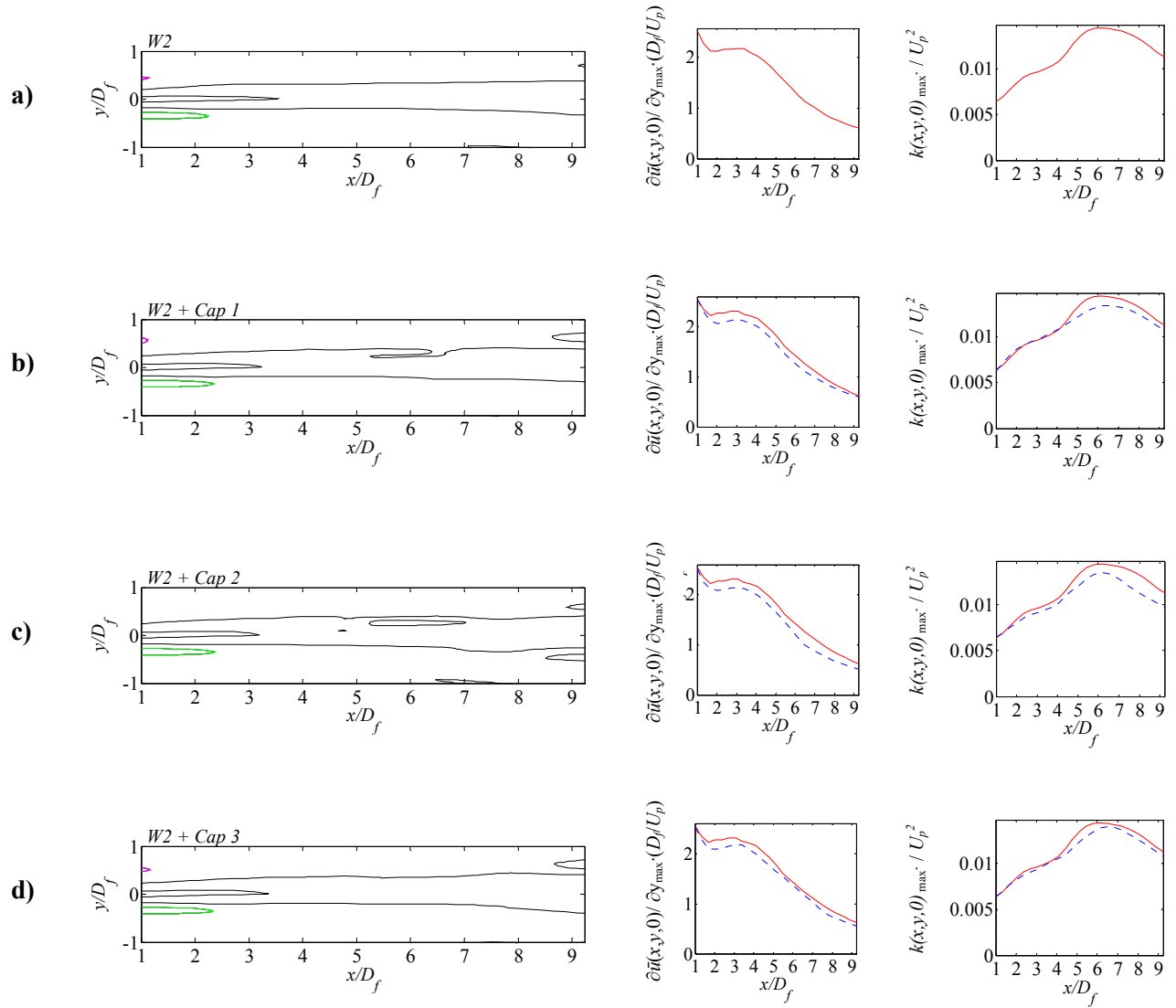
Fig. 16 Inflectional loci showing GSC below jet —— and GSC above jet —— (left); maximum radial gradient of the axial component of mean velocity (middle); and maximum turbulent kinetic energy below jet centerplane (right). a) W_2; b) W_2 + Cap 1; c) W_2 + Cap 2; d) W_2 + Cap 3. (W_2 —— ; W_2 + Caps - - -).

$$\times 10^{-3} \text{ Peak } k \text{ vs. } G \text{ Below & Above Jet Centerline}$$
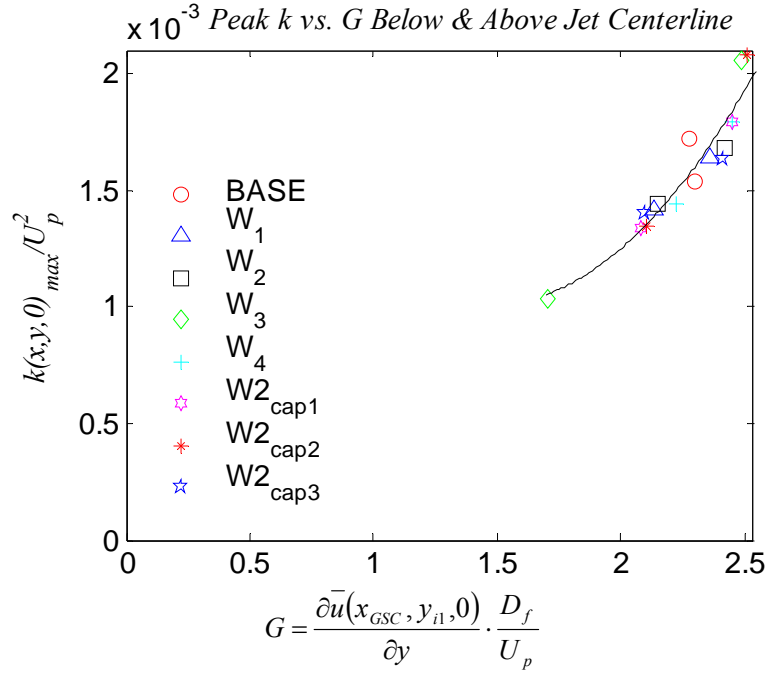
Fig. 17   Correlation of peak TKE versus velocity gradient *G*, valid below and above the jet centerplane. *G* is measured at $x=x_{GSC}$, and it is non-dimensionalized using D_f. A second-order polynomial fit is also plotted.

$$\times 10^{-3} \quad \text{Peak } k \text{ vs. } G \text{ Below Jet Centerline}$$
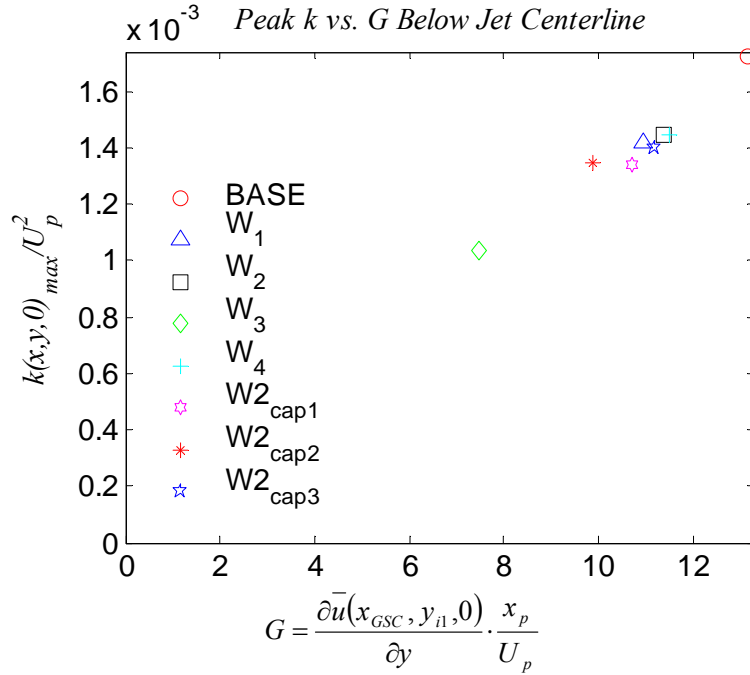
Fig. 18   Correlation of peak TKE versus velocity gradient *G* for the lower half of the jet. *G* is calculated at $x=x_{GSC}$, and it is non-dimensionalized using x_p.

American Institute of Aeronautics and Astronautics